

Received: 16 February 2025 / Accepted: 28 March 2025 / Published online: ----

*protrusion angles,
hollow joint,
THF, numerical simulation*

Nguyen Dac TRUNG¹,
Vu Duc QUANG^{2*}

THE INFLUENCE OF THE PROTRUSION INCLINATION ANGLE ON THE FORMABILITY OF HOLLOW JOINT IN THE TUBE HYDROFORMING PROCESS

Hollow joints formed through the tube hydroforming process offer superior advantages over traditional forming methods such as casting, welding, sheet metal bending, and cutting. The protrusion inclination angle of these hollow joints is a critical geometric parameter that directly influences their formability, including material deformation mechanics, wall thickness distribution, structural integrity, and more during the THF process. Optimizing this angle, along with other process parameters like internal fluid pressure load, axial feed, and counter pressure, can lead to significant improvements in the quality and complexity of the formed hollow joints. This paper focuses on studying the impact of three protrusion inclination angles - 45 degrees, 60 degrees, and 90 degrees - on the formability of hollow joints *HJ45*, *HJ60*, and *HJ90*, based on numerical simulations using ABAQUS/CAE software. Output criteria used to analyse and compare the formability of the joints include forming stress distribution (*S*), plastic strain components (*PE*), material flow, wall thickness distribution (*STH*), and protrusion height. The research results can be utilized to enhance the design capabilities of various protrusions in hollow joints, as well as improve the efficiency of the tube hydroforming process in manufacturing products for applications in the automotive and aerospace industries.

1. INTRODUCTION

Tube products fabricated through tube hydroforming process demonstrate high dimensional accuracy due to precise control of wall thickness and geometric precision during the forming process [1 – 4]. Tube hydroforming enhances material properties via work-hardening effects during forming, reducing weaknesses like thinning seen in other processes like stamping or roll forming [5, 6]. Hydroformed components achieve significant weight reduction compared to welded assemblies, while maintaining structural integrity under stress conditions like impacts [7 – 9]. Production efficiency is significantly improved as traditional steps are consolidated into one operation in tube hydroforming [10, 11]. While initial

¹ Hanoi University of Science and Technology, Hanoi Vietnam

² Faculty of Mechanical Engineering, University of Economics - Technology for Industries, Hanoi Vietnam

* E-mail: vuquang@uneti.edu.vn

<https://doi.org/10.36897/jme/203468>

processing costs may be higher compared to simpler techniques like combined bending/stamping/welding, the long-term benefits are greater when scaled for large-volume production, especially in industries requiring lightweight solutions, such as aerospace and automotive [10].

The protrusion inclination angle (α_P) is a critical parameter in tube hydroforming processes for manufacturing hollow joints, directly influencing the material's formability by affecting material flow, material deformation mechanics, and the structural integrity of the hollow joint. Optimizing this α_P angle is crucial for minimizing wall thinning and ensuring uniform thickness across the protrusion, potentially leading to significant improvements in the quality and complexity of hydroformed tube joints. It affects how the material responds under pressure during hydroforming, where a larger protrusion inclination angle can lead to an increased effective protrusion height, allowing more material to be deformed without failure [11, 12]. Different protrusion inclination angles result in variations in how the tube conforms to the die shape. For instance, studies indicate that employing dual-pressure hydroforming techniques, involving varying pressures on both the inside and outside of the tube, can significantly alter the protrusion formation. This method has been shown to increase the effective protrusion height, suggesting that optimizing protrusion angles in conjunction with pressure variations can lead to improved forming outcomes [13]. The design of the counter punch used in hydroforming processes also plays a role in how protrusion angles affect formability. Research has demonstrated that different head angles of the counter punch can control not only the protrusion height but also the wall thinning during forming. Specifically, an optimal counter punch angle can minimize wall thinning while maximizing protrusion height, indicating that careful consideration of these angles is essential for achieving desired forming results [14].

The α_P angle plays a critical role in determining the thickness distribution within hydroformed hollow joints. It influences how material flows during the hydroforming process, where a larger α_P angle may lead to more pronounced thickness variations across the joint. Specifically, studies have shown that the maximum thickness typically occurs at the base of the protrusion, while the minimum thickness is often located at the apex of the protrusion [15, 16]. This thickness distribution is crucial for ensuring structural integrity and performance under load. The α_P angle affects the material deformation mechanics, where an optimized inclination angle can facilitate a more uniform material flow, reducing localized thinning. For example, research indicates that an optimal α_P angle can minimize tube wall thinning during tube hydroforming of hollow parts, which is essential for maintaining strength and preventing failure in the final product [17, 18].

The Finite Element Method (FEM) has become an indispensable tool for simulating tube hydroforming processes due to its ability to model complex physical phenomena with high accuracy. By numerically simulating the hydroforming process, FEM eliminates the need for costly experimentation and physical prototypes, significantly reducing development time and costs. FEM enables the accurate modelling of material properties and their behavior under multiaxial loading conditions, which is crucial in tube hydroforming. For instance, constitutive models such as the CPB06 and Kim–Tuan hardening models can be integrated into FEM simulations to capture the specific plastic flow behavior of materials like titanium or aluminum [19, 20]. FEM supports iterative optimization processes by allowing engineers

to test various boundary conditions, material properties, or tool designs without physical intervention. It facilitates intermediate optimizations using 2D simulations followed by more detailed 3D analyses for final validation. This capability ensures that engineers can predict potential defects such as wrinkling, tearing, or thinning before actual production.

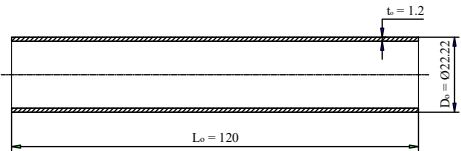
In this study, the authors utilized the FEM with Abaqus/Explicit 3DEXPERIENCE R2017X software to investigate the formability of protrusions in three CDA110 copper alloy hollow joint components using tube hydroforming technology. The components analyzed include *HJ45* (with a protrusion inclination angle of $\alpha_P = 45^\circ$), *HJ60* ($\alpha_P = 60^\circ$), and *HJ90* ($\alpha_P = 90^\circ$). The formability was evaluated based on five criteria: forming stress, plastic strain components, material flow, section thickness, and protrusion height. This analysis facilitates the selection of the lug inclination angle α_P for designing and manufacturing various types of CDA110 copper alloy hollow joints.

2. MATERIALS AND METHODS

2. 1. GEOMETRIC SHAPE AND MATERIAL PROPERTIES OF THE CDA110 TUBE BLANK

The geometric shape and dimensions of the tube blank used for the geometric modelling in Abaqus software are detailed in Table 1. The material properties of the CDA110 tube blank used for the material modelling in Abaqus software are summarized in Table 2. CDA110 is an ideal material for thermal and mechanical applications due to its combination of high thermal conductivity, strain hardening capability, and corrosion resistance. CDA110 tube plays a crucial role in air conditioning equipment, enhancing the efficiency and durability of the system.

Table 1. Geometric Shape of the CDA110 Tube Blank

Parameters	Symbol/unit	Value
		
Outside diameter of tube	D_0 (mm)	22.22
Inside diameter of tube	d_I (mm)	19.82
Initial thickness of tube	t_0 (mm)	1.2
Initial length of tubular blank	L_0 (mm)	120

2.2. TUBE BLANK AND FORMING DIE MODELS

The geometric model, material model, and mesh model of the CDA110 tube blank for all three tube hydroforming processes creating the three types of connectors *HJ45*, *HJ60*, and *HJ90* via numerical simulation were set up identically (Fig. 1). Accuracy and convergence of the FE simulation were ensured by defining the tube blank as a deformable body and meshing

it in the Mesh Module with Global Seeds (46,521 nodes), 46,352 Quad elements, a Free meshing technique, and the Medial Axis algorithm.

Table 2. Material Properties of the CDA110 Tube Blank

Material parameters and properties	Value
Temperature ($^{\circ}\text{C}$)	24
Density, ρ (kg/m^3)	8940
Young's modulus, E (GPa)	115
Hardening coefficient, K (MPa)	325
Work hardening exponent, n	0.54
Poisson's ratio, ν	0.33
Yield strength, σ_Y (MPa)	170
Ultimate tensile strength, σ_U (MPa)	425
Elongation (%)	45

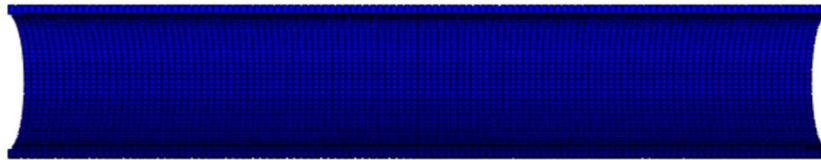


Fig. 1. Identical model settings for the forming simulation of hollow connectors *HJ45*, *HJ60*, and *HJ90*

The forming dies for the three hollow connectors *HJ45*, *HJ60*, and *HJ90* have leftward fillet radii (R_{lf}) and rightward fillet radii (R_{rf}) in the transition regions, detailed in Tab. 3 and modeled as shown in Fig. 2. The assembly module for the numerical simulation consists of four components: a rigid die, a rigid left punch, a rigid right punch, and a deformable tube blank (Fig. 2).

Table 3. Geometric parameters of the forming die

Hollow Joint	Inclined angle of the protrusion α_p ($^{\circ}$)	Guiding zone	Transition zone		Expansion zone
			Leftward fillet radius R_{lf} (mm)	Rightward fillet radius R_{rf} (mm)	
<i>HJ45</i>	45	Includes the region bounded by the right axial punch and the transition zone, and the region bounded by the left axial punch and the transition zone.	15	5	Profiled protrusion forming region
<i>HJ60</i>	60		15	5	
<i>HJ90</i>	90		5	5	

2.3. BOUNDARY CONDITIONS

The internal fluid pressure (the working fluid can be either an oil-based or water-based emulsion) at which the tube begins to undergo plastic deformation, P_Y , when the axial force is zero, can be preliminarily determined according to equation (1) [22]:

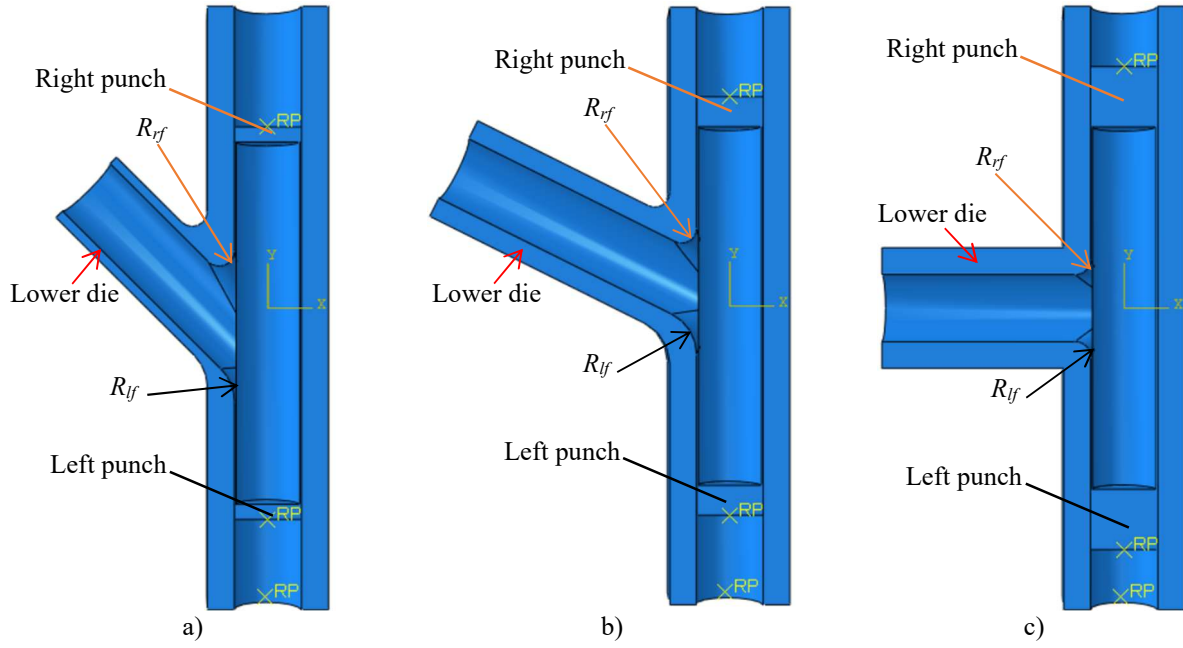


Fig. 2. Assembly of the tube blank model and die for forming hollow joints: a) *HJ45*, b) *HJ60*, c) *HJ90*

$$P_Y = \left(\frac{2t_0}{D_0 - 2t_0} \right) \sigma_Y \quad (1)$$

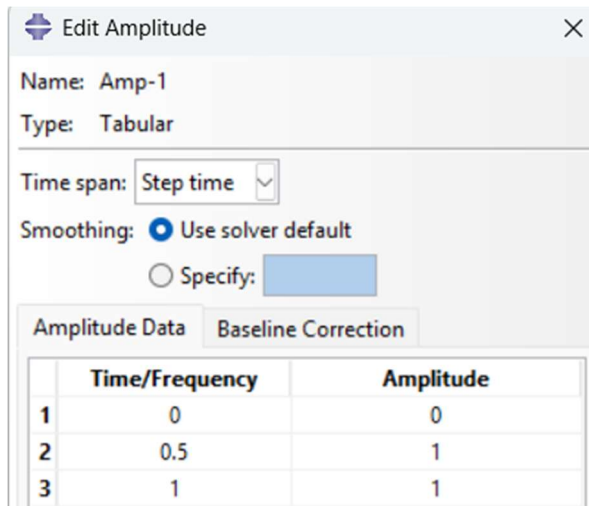
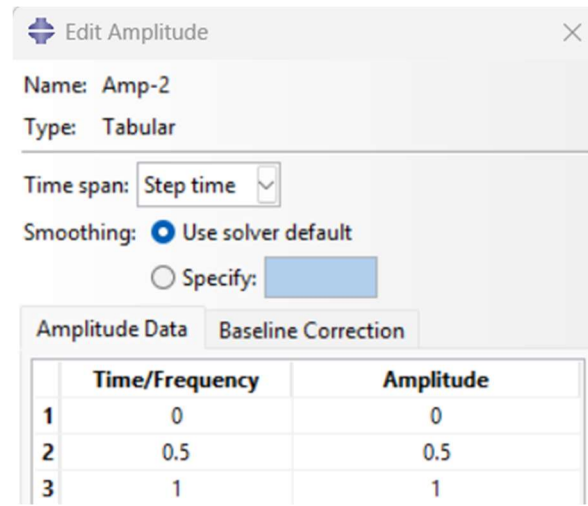
The axial force at which the tube begins to undergo plastic deformation, F_Y , when the internal fluid pressure is zero, can be preliminarily determined according to equation (2) [21]:

$$F_Y = \pi t_0 (D_0 - t_0) \sigma_Y \quad (2)$$

To predict the internal pressure P_b at the onset of rupture during the free plastic deformation stage of hydroforming hollow joint components *HJ45*, *HJ60*, and *HJ90*, equation (3) [22] can be applied:

$$P_b = \sigma_U \left(\frac{2t_0}{D_0 - t_0} \right) \quad (3)$$

Using the values of $\sigma_Y = 170$ MPa, $\sigma_U = 425$ MPa, $t_0 = 1.2$ mm, and $D_0 = 22.22$ mm from Tables 1 and 2, we determined the fluid pressure inside the tube $P_Y = 20.61$ MPa, axial force $F_Y = 13460$ N, and internal pressure at the onset of tearing during free plastic deformation $P_b = 48.57$ MPa, according to equations (1), (2), and (3), prior to conducting numerical and experimental investigations of the tube hydroforming process. The hydroforming process was simulated by simultaneously applying working fluid pressure P_i and axial feeding Af from both ends of the tube symmetrically. The maximum fluid pressure $P_{i-max} = 45$ MPa was set according to the load path Amp-1 as shown in figure 3, and axial feeding $Af = 30$ mm at each end of the tube followed the load path Amp-2 as shown in figure 4, with a friction coefficient of 0.1 between surfaces. These boundary conditions were set uniformly to evaluate and compare the formability of three hollow joints *HJ45*, *HJ60*, and *HJ90*.

Fig. 3. Fluid pressure P_i amplitude as a function of timeFig. 4. Amplitude of axial feeding A_f over time

3. RESULTS AND DISCUSSION

Based on the data obtained from the numerical simulation results of the investigated cases with identical boundary conditions, the authors conducted a detailed analysis and comparison based on five output criteria. This was done to evaluate the formability of the hollow joints *HJ45*, *HJ60*, and *HJ90*.

3.1. FORMING STRESS DISTRIBUTION (S)

The forming stress distribution on each hollow joint component is shown in Fig. 5. Finite element simulations indicated that this stress is not uniform throughout the entire structure but varies significantly depending on specific regions of each hollow joint during the forming process. The forming stress distribution on *HJ90* is balanced in all three regions (Fig. 5c and 6c; the guiding zone and transition zone experience compressive stress with a maximum value of $S_{max-HJ90} = 425$ MPa (indicated in red), while the expansion zone experiences tensile stress with an average value of approximately $S_{a-HJ90} = 250$ MPa. In contrast, the forming stress distribution on *HJ45* (Fig. 5a and 6a) and *HJ60* (Fig. 5b and 6b) differs in all three regions as well as within each individual region. The guiding zone and the transition zone on the right side of joints *HJ45* and *HJ60* experience compressive stress with a maximum value of $S_{max-r-HJ45} = S_{max-r-HJ60} = 425$ MPa, which is greater than that on the left side, where the maximum value is $S_{max-l-HJ45} = S_{max-l-HJ60} = 400$ MPa. Due to the different draft angles of the protrusions of the three hollow joints, both the expansion zone and their forming stress distributions also differ (Fig. 5 and 6).

The distribution of stress along the tube wall on the protrusion forming side, from right to left of the three hollow joint components, varies significantly (as shown in detail in the diagrams in Fig. 6). The forming stress distribution on the tube wall on the protrusion forming side of the *HJ90* hollow joint is more balanced compared to the *HJ45* and *HJ60* hollow joints.

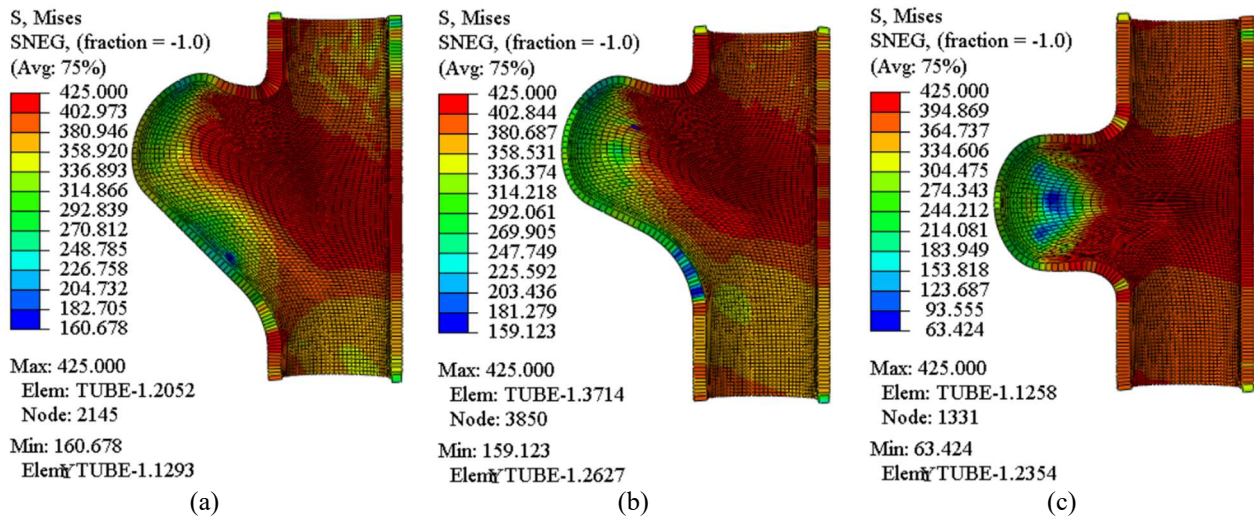


Fig. 5. Forming stress distribution on the hollow joint component: (a) HJ45, (b) HJ60, (c) HJ90

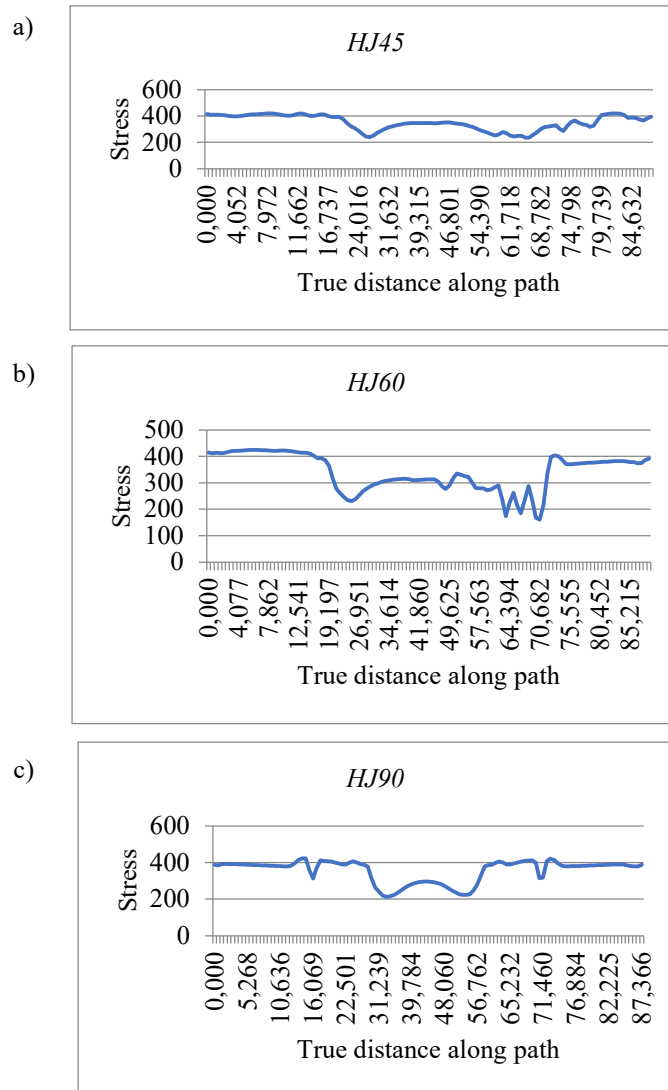


Fig. 6. Forming stress distribution along the tube wall on the protrusion side, from right to left, of the hollow joint component: a) HJ45, b) HJ60, c) HJ90

Meanwhile, the distribution of compressive stress along the tube wall on the side opposite the protrusion being formed shows little variation for all three hollow joints (as shown in detail in Fig. 5).

3.2. PLASTIC STRAIN COMPONENTS (PE)

The plastic strain (PE) components on the three hollow joint components, $HJ45$, $HJ60$, and $HJ90$, are shown in detail in Fig. 7a, 7b, and 7c, respectively. These figures help us understand the nonlinear plastic deformation behavior of the material under three different protrusion inclination angles. The strain components in the guiding zones of all three hollow joints have negative values (Fig. 7 and 8), indicating elastic recovery after unloading due to significant compressive stress during the forming process. In the transition and expansion zones of all three joints, the majority of the strain components have positive values, indicating the permanent plastic deformation that the material undergoes when subjected to stress exceeding its yield strength (Fig. 7 and 8). The maximum values of the strain components are found in both the transition and expansion zones of the $HJ45$ ($PE_{max-HJ45}^P = 0.310$) (Fig. 7a) and $HJ60$ ($PE_{max-HJ60} = 0.770$) (Fig. 7b) hollow joint components. Meanwhile, the maximum value of the strain components is only found in the transition zone of the $HJ90$ hollow joint component ($PE_{max-HJ90} = 0.768$) (Fig. 7c), which is smaller than the maximum value of the $HJ45$ and $HJ60$ hollow joint components. The distribution of plastic strain components on the $HJ90$ hollow joint component is more balanced and smaller compared to the $HJ45$ and $HJ60$ hollow joint components.

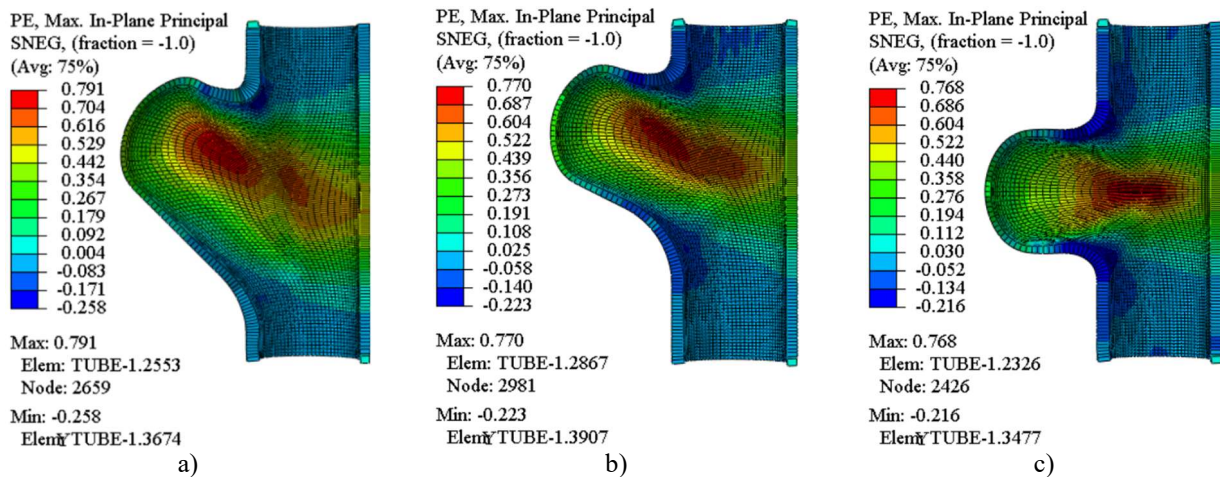


Fig. 7. Distribution of plastic strain components on the hollow joint component: a) $HJ45$, b) $HJ60$, c) $HJ90$

The plastic strain components along the tube wall on the side opposite the protrusion being formed show little variation for all three hollow joints $HJ45$, $HJ60$, and $HJ90$ (as shown in detail in Fig. 7). In contrast, the plastic strain components along the tube wall on the protrusion side, from right to left of these three hollow joint components, have very different distributions (as shown in detail in the diagrams in Fig. 8). The plastic strain components on the tube wall of the $HJ90$ hollow joint component are more balanced, and the maximum value

at the protrusion peak ($PE^P_{max-HJ90} = 0.264$) (Fig. 8c) is smaller compared to the maximum plastic strain components of the HJ45 ($PE^P_{max-HJ45} = 0.388$) (Fig. 8a) and HJ60 ($PE^P_{max-HJ60} = 0.310$) (Fig. 8b) hollow joint components.

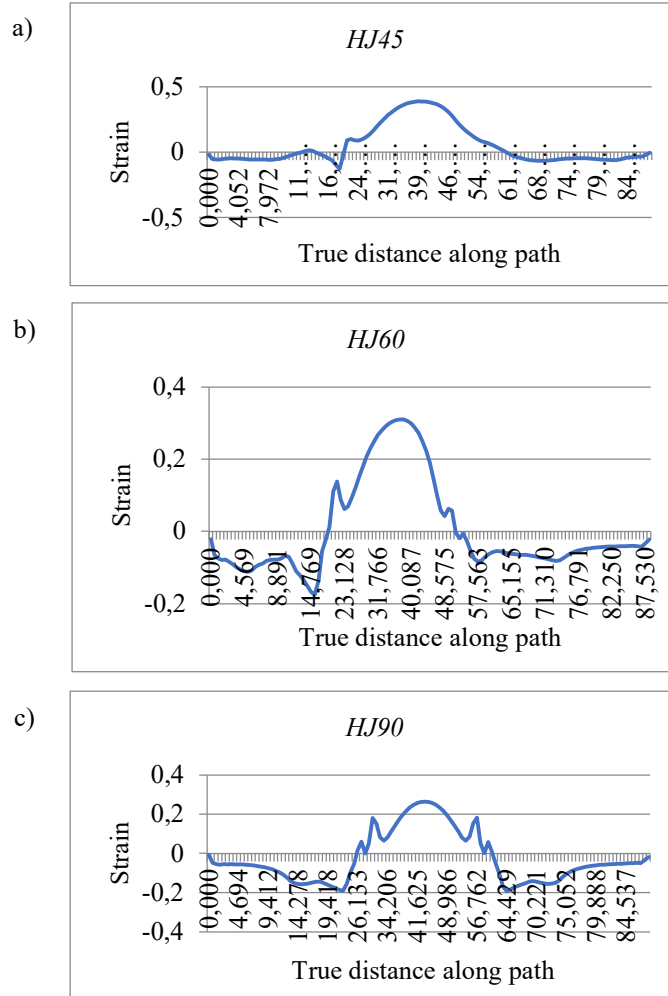


Fig. 8. Plastic strain components along the tube wall on the protrusion side, from right to left, of the hollow joint component: a) HJ45, b) HJ60, c) HJ90

3.3. MATERIAL FLOW

The material flow along the die cavity profile during hydroforming of the tube blank to form the three hollow joint components HJ45, HJ60, and HJ90 is generated by the axial force component from both ends of the tube blank (left axial punch and right axial punch) and the internal fluid pressure, as shown in detail in Fig. 9. The forming results show that the outer surface profiles of the HJ60 (Fig. 9b) and HJ90 (Fig. 9c) hollow joints meet the required left and right corner radii. The outer surface profile of the HJ45 hollow joint (Fig. 9a) meets the required left corner radius $R_{lf} = 15\text{mm}$, but its outer surface profile does not meet the required right corner radius $R_{rf} = 5\text{mm}$. Increasing the internal fluid pressure P_i to achieve the required

outer surface profile at the right corner radius may pose a significant risk of severe thinning of the tube wall thickness at the protrusion peak, leading to rupture failure. To overcome this risk, counter pressure and lubrication can be used during the forming process. On the side opposite the protrusion being formed, the tube wall is subjected to axial compression due to the axial force from the left and right axial punches acting on both ends of the tube blank, and the internal fluid pressure forces the tube wall to conform to the die cavity profile.

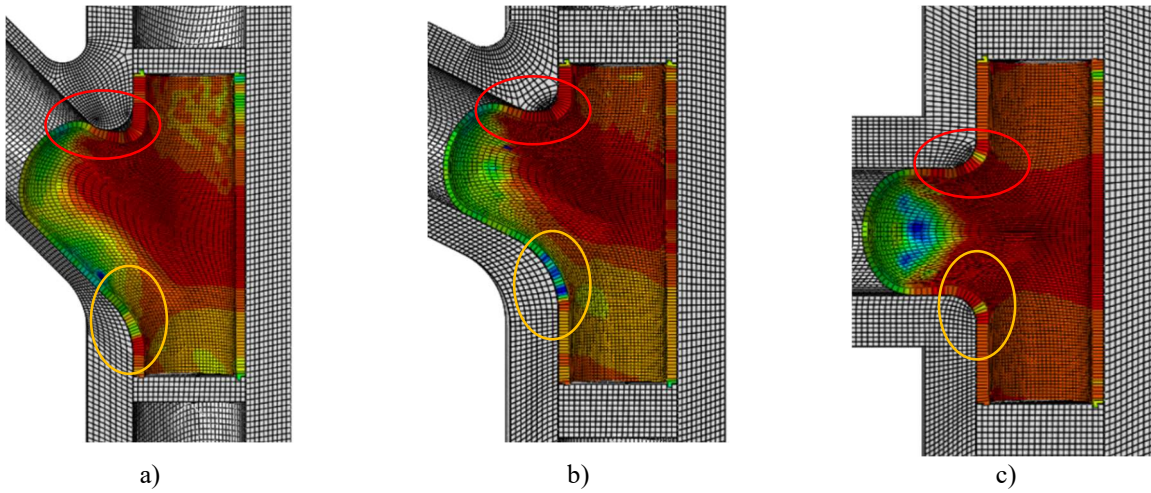


Fig. 9. Material flow along the die cavity profile during hydroforming of the hollow joint component: a) *HJ45*, b) *HJ60*, c) *HJ90*

3.4. TUBE WALL THICKNESS DISTRIBUTION (*STH*)

The tube wall thickness (*STH*) distribution in the formed hollow joints is non-uniform due to stretching or compression during the forming process (Fig. 10, Fig.11). Tube wall thinning only occurs in the expansion zone. According to the allowable thinning limit of the tube wall, $\varepsilon_{max} = 30\%$ (equivalent to a minimum tube wall thickness $STH_{min} = 0.84$ mm), all three formed joints meet the requirement. However, analyzing the tube wall thickness distribution along the longitudinal section of the *HJ45* (Fig. 11a), *HJ60* (Fig. 11b), and *HJ90* (Fig. 11c) hollow joint components reveals that their guiding and transition zones are thickened. In the transition zone with a radius of $R = 5$ mm, the *HJ45* hollow joint achieves $STH_{max-HJ45-R5} = 2.985$ mm, followed by the *HJ60* joint with $STH_{max-HJ60-R5} = 2.963$ mm, and finally the *HJ90* joint with $STH_{max-HJ90-R5} = 2.591$ mm. In the transition zone with a radius of $R = 15$ mm, the *HJ45* hollow joint has a thickness of $STH_{max-HJ45-R15} = 2.985$ mm, which is greater than the thickness of the *HJ60* hollow joint, $STH_{max-HJ60-R15} = 2.962$ mm. Meanwhile, in the expansion zone, the *HJ45* hollow joint has the smallest thickness, $STH_{min-HJ45} = 0.873$ mm, followed by the *HJ60* hollow joint with $STH_{min-HJ60} = 0.957$ mm, and finally the *HJ90* hollow joint with the largest thickness, $STH_{min-HJ90} = 1.009$ mm. Overall, according to the diagrams in Fig. 10a, b, and c, the *HJ90* hollow joint has the most reasonable and balanced tube wall thickness distribution, followed by the *HJ60* hollow joint, and the least reasonable is the *HJ45* hollow joint. The tube wall on the side opposite the protrusion of all three hollow joint components is thickened, with an average increase of approximately 100% compared to the initial tube blank thickness t_0 .

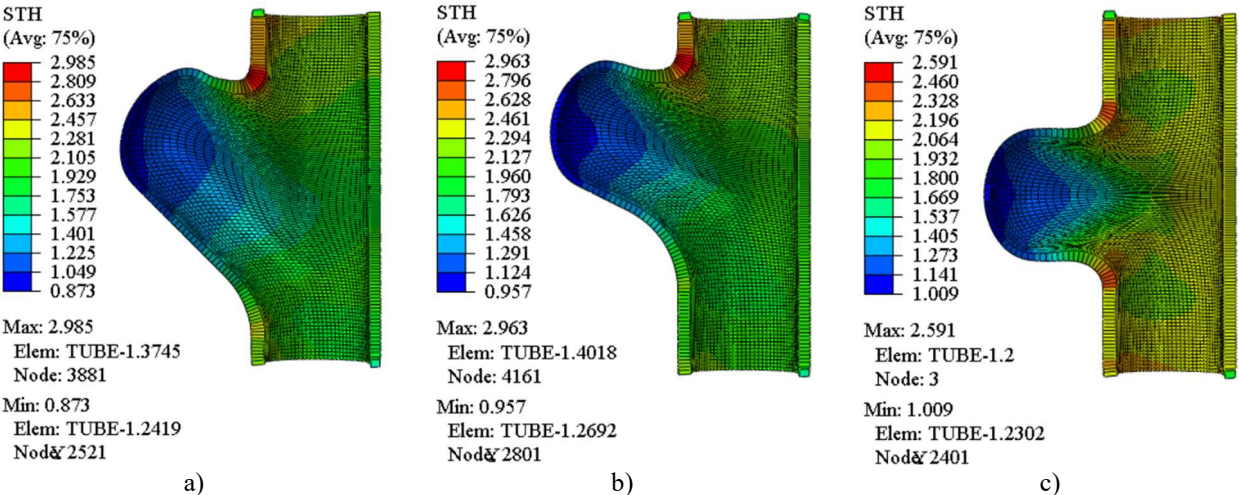


Fig. 10. Tube wall thickness (STH) distribution of the hollow joint component: a) HJ45, b) HJ60, c) HJ90

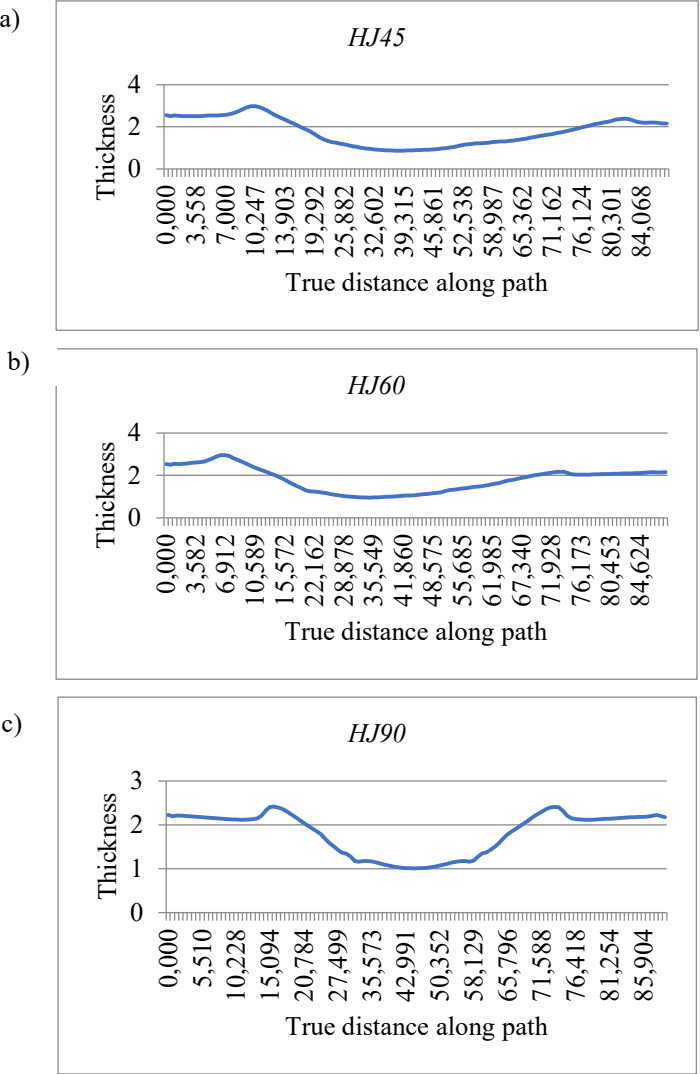


Fig. 11. Tube wall thickness (STH) distribution on the protrusion forming side, from right to left, of the hollow joint component: a) HJ45, b) HJ60, c) HJ90

3.5. PROTRUSION HEIGHT

The maximum height of the protrusion (UI^P_{max}) for the hollow joint parts *HJ45*, *HJ60*, and *HJ90* is relatively similar: $UI^P_{max-HJ45} = |-22.601|$ mm (Fig. 12a), $UI^P_{max-HJ60} = |-21.553|$ mm (Fig. 12b), and $UI^P_{max-HJ90} = |-19.935|$ mm (Fig. 12c). Meanwhile, there is a significant difference in the maximum thinning ratio (ϵ_{max}) of the tube wall at the maximum height of the protrusion among the three hollow joint parts, specifically: $\epsilon_{max-HJ45} = 27.25\%$, $\epsilon_{max-HJ60} = 20.25\%$, and $\epsilon_{max-HJ90} = 15.92\%$. This maximum thinning ratio (ϵ_{max}) may lead to considerable differences in the effective height (UI^P_e) of the three formed hollow joint parts. The effective height (UI^P_e) is intended to ensure that the formed protrusion meets design specifications and industrial quality standards regarding durability and stiffness.

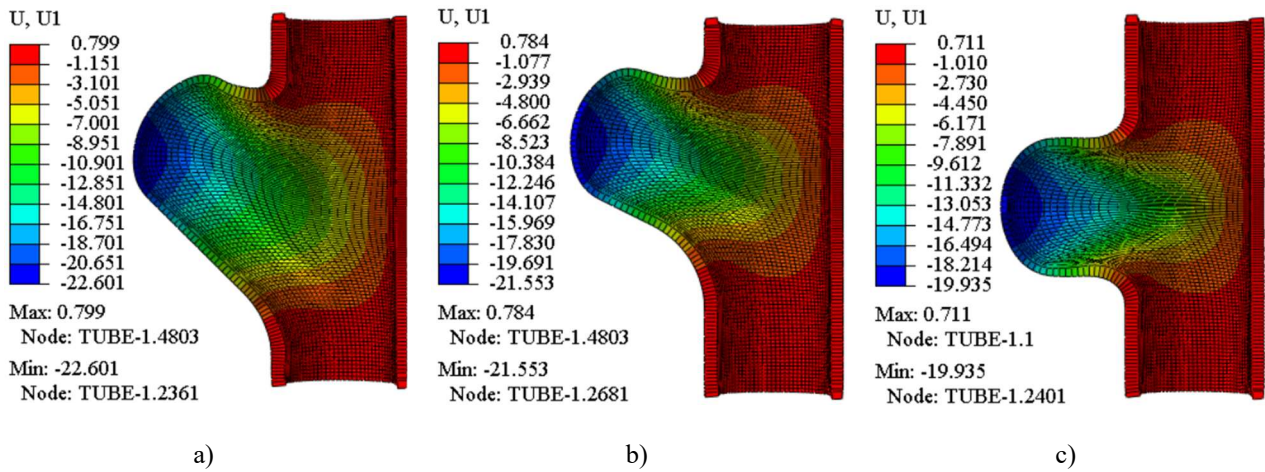


Fig. 12. Height of the protrusion (UI) of the formed hollow joint parts: a) *HJ45*, b) *HJ60*, c) *HJ90*

4. CONCLUSION

This study successfully explored the influence of the protrusion inclination angle α_P on the formability of hollow joint variants *HJ45*, *HJ60*, and *HJ90* using tube hydroforming through advanced numerical simulation in ABAQUS/CAE software. The evaluation of the formability of the three hollow joints according to five key criteria - Mises equivalent stress distribution, plastic strain components, material flow, section thickness distribution, and protrusion height - revealed critical insights into the relationship between the inclination angle α_P and forming performance.

The results demonstrate that the inclination angle α_P profoundly impacts all five output criteria, with hollow joints *HJ60* and *HJ90* exhibiting more uniform stress profiles and reduced localized thinning compared to *HJ45*. Conversely, the *HJ45* hollow joint showed a higher susceptibility to excessive plastic deformation and material flow irregularities, highlighting the importance of selecting an optimal inclination angle α_P to minimize defects. The analysis confirmed that larger inclination angles α_P (e.g., the *HJ90* hollow joint) enhance

dimensional stability and maintain tube wall thickness, while intermediate angles (e.g., the HJ60 hollow joint) balance formability and structural integrity. These findings underscore the critical role of geometric design in tube hydroforming processes and provide a data - driven framework for optimizing hollow joint production.

The research advocates the integration of numerical simulations into industrial applications to predict forming outcomes and refine process parameters. Future research could extend this work by further exploring alternative angles, materials, or multi - stage forming strategies to further enhance the efficiency and reliability of hydroformed components.

REFERENCES

- [1] ENDELT B., 2022, *In-Process Feedback Control of Tube Hydro-Forming Process*, The International Journal of Advanced Manufacturing Technology, 119, 7723–7733.
- [2] XU Y., ZHANG X., XIE W., ZHANG S., HUANG X., TIAN Y., CHEN L., 2024, *Fuzzy Control Optimization of Loading Paths for Hydroforming of Variable Diameter Tubes*, Computers, Materials & Continua, 81/2, 2753–2768.
- [3] REDDY P.V., REDDY B.V., RAMULU P.J., 2020, *Evolution of Hydroforming Technologies and its Applications—a Review*, J. Adv. Manuf. Syst., 19, 737–780.
- [4] BELL C., CORNEY J., ZUELLI N., SAVINGS D., 2020, *A State of the Art Review of Hydroforming Technology*, Int. J. Mater. Form., 13, 789–828.
- [5] YUENYONG J., SUTHON M., KINGKLANG S., THANAKIKASEM P., MAHABUNPHACHAI S., UTHAISANGSUK V., 2017, *Formability Prediction for Tube Hydroforming of Stainless Steel 304 Using Damage Mechanics Model*, Journal of Manufacturing Science and Engineering, 140/1, 011006.
- [6] OMAR A., TEWARI A., NARASIMHAN K., 2015, *Formability and Microstructure Evolution During Hydroforming of Drawing Quality Welded Steel Tube*, The Journal of Strain Analysis for Engineering Design, 50/7, 542–556.
- [7] ROSENTHAL S., MAAB F., KAMALIEV M. et al., 2020, *Lightweight in Automotive Components by Forming Technology*, Automot. Innov., 3, 195–209.
- [8] CRISTELLO N., KIM, I.Y., 2007, *Multidisciplinary Design Optimization of a Zero-Emission Vehicle Chassis Considering Crashworthiness and Hydroformability*, Proceedings of the Institution of Mechanical Engineers, Part D: Journal of Automobile Engineering, 221/5, 511–526.
- [9] ZHAO X., KONG C., YANG Y., HAGIWARA I., 2022, *Reversed-Torsion-Type Crush Energy Absorption Structure and its Inexpensive Partial-Heating Torsion Manufacturing Method Based on Origami Engineering*, Manuf. Sci. Eng., 144/6, 061001.
- [10] CHINCHANIKAR S., MULIK H., VARUDE P., et al., 2024, *A Review of Emerging Hydroforming Technologies: Design Considerations, Parametric Studies, and Recent Innovations*, J. Eng. Appl. Sci., 71, 205.
- [11] NGAILE G., AVILA M., 2023, *Improving Material Formability and Tribological Conditions Through Dual-Pressure Tube Hydroforming*, Journal of Manufacturing and Materials Processing, 7/4, 126.
- [12] NGAILE G., AVILA M., 2022, *Tribological Characteristics of Dual-Pressure Tube Hydroforming*, Defect and Diffusion Forum, 414, 111–116.
- [13] QUANG V.D., DUY D.V., TRUNG N.D., QUANG N.H., 2022, *Quality Comparison of Y-Shape Joints by Tube Hydroforming with and without Counterforce*, EUREKA: Physics and Engineering, 4/4, 46–56.
- [14] TENG B., LIU G., YUAN S., 2013, *Effect of End Angle of Counterpunch on Y-Shape Hydroforming*, Advanced Materials Research, 753–755, 1539–542.
- [15] VU D.Q., NGUYEN D.T., CHU V.H., NGUYEN H.T., NGUYEN A.T., NGUYEN Q.H., 2024, *Study on the Effect of Internal Pressure and Axial Feed in Tube Hydrostatic Forming Process of T-Shaped Joints*, Long, B.T., et al. Proceedings of the 3rd Annual International Conference on Material, Machines and Methods for Sustainable Development (MMMS2022). MMMS 2022, Lecture Notes in Mechanical Engineering, 2, 379–391.
- [16] QUANG V.D., TRUNG N.D., NAM D.H., VAN TRUC, N., 2024, *Comparison of Axial Feed Options in Tube Hydrostatic Forming Process to the Quality of 60° Y-Shaped Components Made of CDA110 Copper*, Long, B.T., et al. Proceedings of the 3rd Annual International Conference on Material, Machines and Methods for Sustainable Development (MMMS2022), MMMS 2022, Lecture Notes in Mechanical Engineering, 2, 393–404.
- [17] KARAMI J.S., PAYGANEH G., KHODSETAN M., 2019, *Numerical and Experimental Study of Residual Stress Measurement and Thickness Distribution of T-Shape Steel Tube Produced by Tube Hydroforming*, Journal of Modern Processes in Manufacturing and Production, 8/1, 45–58.
- [18] TENG B., LIU G., YUAN S., 2013, *Effect of End Angle of Counterpunch on Y-Shape Hydroforming*, Advanced Materials Research, 753–755, 1539–1542.

- [19] CHENG L., GUO H., SUN L., YANG C., SUN F., LI J., 2024, *Real-Time Simulation of Tube Hydroforming by Integrating Finite-Element Method and Machine Learning*, Journal of Manufacturing and Materials Processing, 8/4, 175.
- [20] PHAM Q.T., LE H.S., NGUYEN A.T., et al., 2022, *A Machine Learning–Based Methodology for Identification of the Plastic Flow in Aluminum Sheets During Incremental Sheet Forming Processes*, Int. J. Adv. Manuf. Technol., 120, 3559–3584.
- [21] ASNAFI N., 1999, *Analytical Modelling of Tube Hydroforming*, Thin-Walled Structures, 34, 295–330.
- [22] KOÇ M., 2008, *Hydroforming for Advanced Manufacturing*, 1st ed, Woodhead Publishing Limited, Cambridge, England.